Magnetic resonance image reconstruction from undersampled measurements using a patch-based nonlocal operator

Xiaobo Qu[1]*, Yingkun Hou[2], Fan Lam[3], Di Guo[4], Jianhui Zhong[5], Zhong Chen[1]*

[1]*Department of Electronic Science, Fujian Provincial Key Laboratory of Plasma and Magnetic Resonance, State Key Laboratory of Physical Chemistry of Solid Surfaces, Xiamen University, Xiamen 361005, China*
[2]*School of Information Science and Technology, Taishan University, Taian 271021, China*
[3]*Department of Electrical and Computer Engineering, University of Illinois at Urbana-Champaign, Urbana, IL 61801, USA*
[4]*School of Computer and Information Engineering, Xiamen University of Technology, Xiamen 361024, China*
[5]*Department of Imaging Sciences, University of Rochester, Box 648, Elmwood Avenue, Rochester, NY 14642-8648, USA*
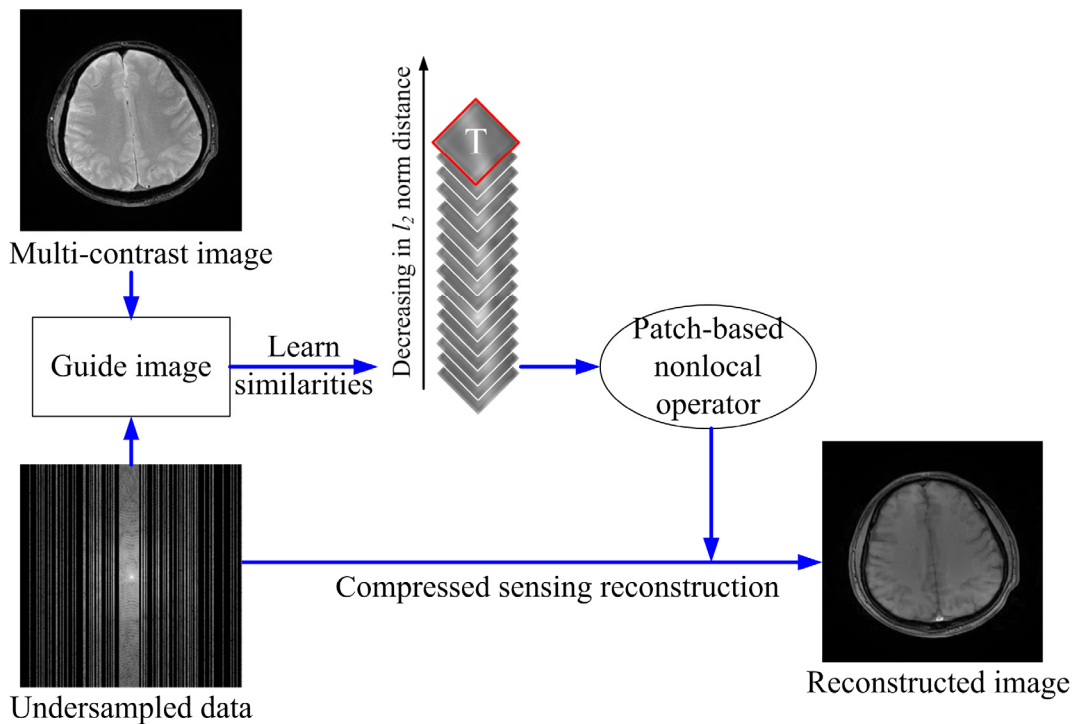
Abstract

Compressed sensing MRI (CS-MRI) has shown great potential in reducing data acquisition time in MRI. Sparsity or compressibility plays an important role to reduce the image reconstruction error. Conventional CS-MRI typically uses a pre-defined sparsifying transform such as wavelet or finite difference, which sometimes does not lead to a sufficient sparse representation for the image to be reconstructed. In this paper, we design a patch-based nonlocal operator (PANO) to sparsify magnetic resonance images by making use of the similarity of image patches. The definition of PANO results in sparse representation for similar patches and allows us to establish a general formulation to trade the sparsity of these patches with the data consistency. It also provides feasibility to incorporate prior information learnt from undersampled data or another contrast image, which leads to optimized sparse representation of images to be reconstructed. Simulation results on in vivo data demonstrate that the proposed method achieves lower reconstruction error and higher visual quality than conventional CS-MRI methods.

Keywords：Magnetic resonance imaging, image reconstruction, compressed sensing, sparsity, nonlocal operator, similarity measurement.

*Corresponding authors: quxiaobo@xmu.edu.cn (X. Qu), chenz@xmu.edu.cn (Z. Chen)

Highlights

Multi-contrast image

Guide image

Learn similarities

Decreasing in l_2 norm distance

T

Patch-based nonlocal operator

Undersampled data

Compressed sensing reconstruction

Reconstructed image

- A patch-based nonlocal operator (PANO) to model the sparse representation of similar image patches is proposed.

- PANO provides feasibility to incorporate prior information learnt from undersampled data or another contrast image.

- PANO-based undersampled magnetic resonance image reconstruction method is proposed.

- Simulations are performed on *in vivo* data and PANO is compared with typical compressed sensing MRI methods.

PANO achieves lower reconstruction error and higher visual quality than the compared methods.

1. Introduction

Magnetic resonance imaging (MRI) is widely used in the clinical diagnosis but limited by its data acquisition speed. Reducing the number of measurements required by Nyquist sampling theorem is one way to accelerate the data acquisition at the cost of introducing aliasing artifacts in the reconstructed images. As a promising method, compressed sensing (Candes et al., 2006; Donoho, 2006) has been introduced for magnetic resonance (MR) image reconstruction [3], called compressed sensing MRI (CS-MRI), from limited data by regularizing the image with $\ell_p \left(0 \leq p \leq 1 \right)$ norm assuming MR images are sparse/highly compressible in a certain transform domain, e.g. wavelet (Block et al., 2007; Haldar et al., 2011; Huang et al., 2012; Huang et al., 2011; Lustig et al., 2007; Majumdar and Ward, 2011), contourlet (Gho et al., 2010; Qu et al., 2010b), finite difference domains (Bilgic and Adalsteinsson, 2012; Bilgic et al., 2011; Block et al., 2007; Haldar et al., 2011; Huang et al., 2012; Huang et al., 2011; Lustig et al., 2007; Trzasko and Manduca, 2009). For the cardiac imaging, the temporal sparsity is represented with Fourier transform (Gamper et al., 2008; Jung et al., 2009; Otazo et al., 2010) and combined with low-rank strcture (Lingala et al., 2011; Zhao et al., 2012). Some of these transforms have been combined to further improve the reconstruction (Huang et al., 2011; Lustig et al., 2007; Qu et al., 2010a). Dictionary trained from the intermediate reconstruction or fully sampled reference images have also been introduced for MRI reconstruction (Chen et al., 2010; Qu et al., 2012; Ravishankar and Bresler, 2011)(Ning et al. 2013). The trained dictionary is expected to provide sparser representation of MR images than the general sparsifying transforms thus improve the reconstruction. Incorporating prior information by sorting the pixels to enhance the sparsity was evidenced to improve the reconstruction of image details (Adluru and DiBella, 2008; Wu et al., 2011).

Recently, the nonlocal processing (Buades et al., 2005; Dabov et al., 2007) has been introduced for MRI reconstruction to make use of the similarity of image patches (Adluru et al., 2010; Fang et al., 2010; Liang et al., 2011; Wong et al., 2010). These methods make use of the pattern redundancy, which is the root of self-similarity property of the images, to provide sparse representation. In (Adluru et al., 2010; Fang et al., 2010; Liang et al., 2011), the difference between neighboring patches is utilized to provide the weights to penalize the difference between pixels from a large neighborhood. Results in (Adluru et al., 2010; Fang et al., 2010; Huang and Yang , 2012; Liang et al., 2011; Wong et al., 2013) have shown that image details are better preserved compared with the conventional CS reconstruction. Rather than directly penalizing the difference of pixels, the sparsity originated from the similarity of image patches was exploited in block-matching and 3D filtering (BM3D) for image denoising (Dabov et al., 2007), and is introduced to reconstruct images from undersampled Fourier measurements in (Akçakaya et al.,

2011; Egiazarian et al., 2007). It has been shown that edges are better preserved for these methods. Besides the image reconstruction, making use of the pattern redundancy also shows great advantages in denoising (Bao et al., 2013; Manjón et al., 2008; Manjón et al., 2012) and super-resolution (Manjón et al., 2012).

In this paper, making use of similarity in images is taken one step further. We first establish a general patch-based nonlocal operator (PANO) to provide sparse representation of similar patches. The linearity of PANO allows us to establish a general reconstruction formulation and tradeoff between the sparsity of similar patches and the data consistency. This formulation also provides the flexibility to incorporate other knowledge into the reconstruction by adding proper constraints. Since the k-space data is undersampled, no ground truth image is available to learn the similarity. We propose to learn the similarity from a guide image estimated from the undersampled measurements. Simulation results imply that learning the similarity is not sensitive to the initial guide image. Unlike learning the similarities many times in the iterations in (Akçakaya et al., 2011; Egiazarian et al., 2007), repeating this process twice is sufficiently enough in the proposed method. This can save computation in searching similar patches.

The remainder of this paper is organized as follows: The conventional CS-MRI reconstruction is reviewed in Section 2. The definition of PANO, the proposed reconstruction formulation and the numerical algorithm, are presented in Section 3. Reconstruction results using the proposed method and the comparison with conventional CS-MRI methods are analyzed in Section 4. The discussions are presented in Section 5. Finally, the conclusions are given in Section 6.

2. Methodology

2.1. Conventional CS-MRI

Consider the data acquisition model

$$\mathbf{y} = \mathbf{F_U}\mathbf{x} + \boldsymbol{\varepsilon},\tag{1}$$

where $\mathbf{x} \in \mathbb{C}^N$ is the discretized image to be reconstructed, $\mathbf{y} \in \mathbb{C}^M$ is the acquired k-space data, $\mathbf{F_U} \in \mathbb{C}^{M \times N}$ ($M < N$) is the undersampled Fourier transform operator which directly relies on the sampling scheme (Lustig et al., 2007), and $\boldsymbol{\varepsilon} \in \mathbb{C}^M$ is the noise vector, a typical CS-MRI reconstruction attempts to solve the following problem (Lustig et al., 2007):

$$\hat{\mathbf{x}} = \arg\min_{\mathbf{x}} \left\{ \left\| \boldsymbol{\Psi}^T \mathbf{x} \right\|_1 + \frac{\lambda}{2} \left\| \mathbf{y} - \mathbf{F_U}\mathbf{x} \right\|_2^2 \right\},\tag{2}$$

where $\boldsymbol{\Psi}^T$ is a sparsifying transform of $\mathbf{x}$, the $\left\| \cdot \right\|_1$ stands for the ℓ_1 norm, which promotes the sparsity of $\boldsymbol{\Psi}^T \mathbf{x}$, and the $\left\| \cdot \right\|_2$ stands for the ℓ_2 norm, which enforces the fidelity of the reconstruction to the measured k-space data. The regularization parameter λ decides the tradeoff between the sparsity and the data fidelity.

Although CS-MRI is promising for reconstruction from undersampled k-space data, the usage of a pre-defined sparsifying transform sometimes lead to an insufficient sparse representation for certain types of images, thus results in artifacts in the reconstruction. For example, the commonly used 2D separable wavelet fails in capturing smooth contours (Gho et al., 2010; Qu et al., 2010b) and finite difference may introduce staircase artifacts (Knoll et al., 2011; Ying and Jim, 2011) at high undersampling factors. Our aim is to construct a better sparsifying transform by making use of the nonlocal similarity of image patches to achieve higher undersampling factors than conventional CS-MRI.

2.2 Undersampled MR image reconstruction with patch-based nonlocal operator

The proposed method assumes that a guide image is available to give a good estimate of nonlocal similarity for image patches. This nonlocal similarity information is integrated as prior information into the proposed patch-based nonlocal operator (PANO), which is utilized to establish a general reconstruction formulation. The essential component of the proposed method is the design of the PANO. To introduce the concept of PANO, we have to introduce the idea of nonlocal similarity.

2.2.1. Patch-based nonlocal operator

Patch grouping is shown in Fig. 1. For a given image $\mathbf{x} \in \mathbb{C}^N$, we first decompose it into patches with fixed size $L \times L$. Let $\mathbf{P}_i$ defines the patch decomposition, and the ith patch $\mathbf{b}_i \in \mathbb{C}^{L^2}$ is expressed as $\mathbf{b}_i = \mathbf{P}_i \mathbf{x}$. The v_j group of image patches is denoted as $\mathbf{R}_{v_j} \mathbf{b}_i$ where $v_j = \{i_1, \cdots, i_Q\}$ stores the index of patches. Let $\mathbf{\Psi}_{3D}$ be a 3D transform, we define the nonlocal operator PANO as

$$\mathbf{A}_j = \mathbf{\Psi}_{3D} \mathbf{R}_{v_j} \mathbf{P}_i. \tag{3}$$

If only one patch is available in a group, $\mathbf{\Psi}_{3D}$ is reduced to a 2D sparsifying transform, e.g. discrete cosine transform or Haar wavelet transform.

An optimal grouping is that

$$\boldsymbol{\alpha}_j = \mathbf{A}_j \mathbf{x} \tag{4}$$

leads to produce sparse coefficients. The adjoint operator $\mathbf{A}_j^T$ is $\mathbf{A}_j^T = \mathbf{P}_i^T \mathbf{R}_{v_j}^T \mathbf{\Psi}_{3D}^T$ and it satisfies

$$\sum_j^J \mathbf{A}_j^T \mathbf{A}_j = \mathbf{O} = \begin{bmatrix} o_1 & 0 & \cdots & 0 & 0 \\ 0 & \ddots & \vdots & \cdot\cdot\cdot & 0 \\ \vdots & \cdots & o_n & \cdots & \vdots \\ 0 & \cdot\cdot\cdot & \vdots & \ddots & 0 \\ 0 & 0 & \cdots & 0 & o_N \end{bmatrix} \tag{5}$$

if $\mathbf{\Psi}_{3D}$ is an orthogonal transform, where o_n is a counter indicating the times that the nth pixel is grouped into the 3D arrays. Therefore, an image is estimated from PANO coefficients according to

$$\hat{\mathbf{x}} = \mathbf{O}^{-1} \sum_{j=1}^{J} \mathbf{A}_j^T \boldsymbol{\alpha}_j . \tag{6}$$

The invertibility of $\mathbf{O}$ requires that each pixel must be contained in at least one group.
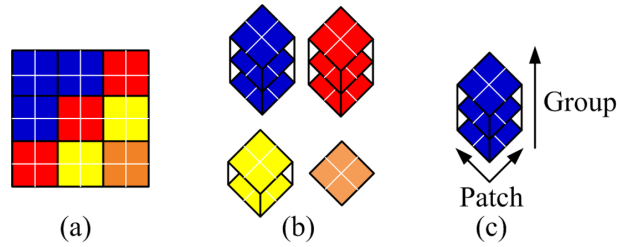
Fig.1. Group image patches. (a) An image with 6×6 pixels; (b) four groups of patches; (c) the patch and group dimension.

2.2.2. Choice of grouping

In this paper, similar patches are grouped to produce sparse coefficients since it shows great potentials to improve the MR image reconstruction (Akçakaya et al., 2011; Egiazarian et al., 2007).

Fig. 2(a) illustrates how to group similar patches. For a search region Ω and the reference patch $\mathbf{T}$, we measure the similarity between the reference patch and a candidate patch using the ℓ_2 norm distance

$$d(\mathbf{T}, \mathbf{b}) = \left\| \mathbf{T}(\mathbf{r}, L) - \mathbf{b}(\tilde{\mathbf{r}}, L) \right\|_2 . \tag{7}$$

$Q - 1$ candidates with the smallest distance are selected as similar patches. This process is called block matching (Dabov et al., 2007). Since the available search region can be as large as the entire image, the similar patches are not limited to a local region. Thus, the similarity is nonlocal.

Performing the 3D Haar wavelet transform on this group, spares coefficients are produced due to the similarity of these patches. An example is shown in Fig. 2. 15 similar patches and the reference patch are grouped in Fig. 2(c). Fig. 2(d) shows that 3D Haar wavelet coefficients of the 3D array decay much faster than the coefficients of 2D Haar wavelet and the pixel values of these patches. This observation implies that 3D Haar wavelets can provide sparser vectors of these grouped patches than 2D Haar wavelets.
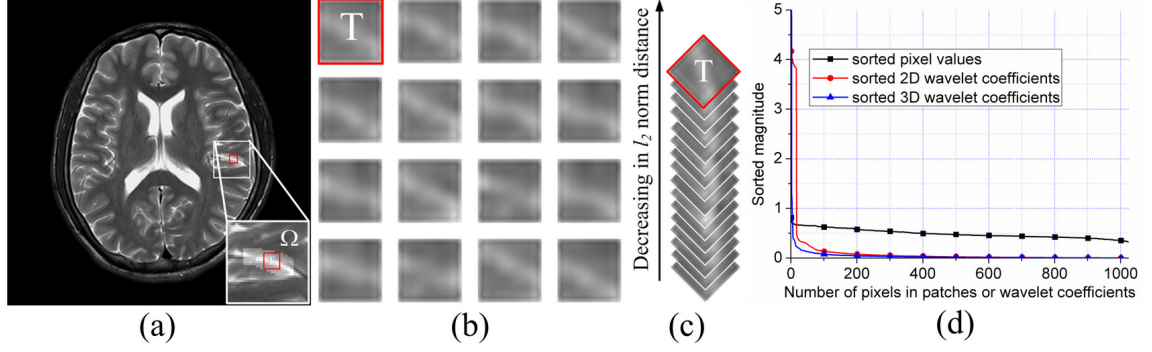
Fig.2. Illustration of the similar patches found via block matching and the sparsity results in. (a) A search region Ω with $D \times D = 39 \times 39$ and the reference patch **T** with $L \times L = 8 \times 8$; (b) $Q = 16$ similar patches found by the ℓ_2 norm distance measure with patch size $L = 8$; (c) 3D array stacked from the similar patches, and (d) curves for decay of pixel values, 2D and 3D wavelet coefficients.

If we rearrange the Q similar patches into a 3D array $\mathbf{B} \in \mathbb{R}^{L \times L \times Q}$ according to the sorted distance d and perform the 3D Haar wavelet transform on this array, a spares vector can be produced due to the similarity of these patches. The entire process is illustrated in Fig. 2. 15 similar patches and the reference patch are grouped in to a 3D array in Fig. 2(c). Fig. 2(d) shows that 3D Haar wavelet coefficients of the 3D array decay much faster than the coefficients of 2D Haar wavelet and the pixel values of these patches. This observation implies that 3D Haar wavelets can provide sparser vectors of these grouped patches than 2D Haar wavelets. This sparsity motivates us to combine grouping similar patches with PANO and introduce this operator in MRI reconstruction that is described in Section 2.2.3.

2.2.3. Undersampled MRI Reconstruction model using PANO

Based on the observation that $\boldsymbol{\alpha}_j$ is sparse when similar patches are grouped, we propose to reconstruct the MR image from undersampled k-space data by solving the following problem

$$\hat{\mathbf{x}} = \arg\min_{\mathbf{x}} \sum_{j=1}^{J} \left\| \mathbf{A}_j \mathbf{x} \right\|_1 + \frac{\lambda}{2} \left\| \mathbf{y} - \mathbf{F}_U \mathbf{x} \right\|_2^2 \tag{8}$$

where the term $\sum_{j=1}^{J} \left\| \mathbf{A}_j \mathbf{x} \right\|_1$ promotes the sparsity and the term $\left\| \mathbf{y} - \mathbf{F}_U \mathbf{x} \right\|_2^2$ enforces the data consistency. λ trades the sparsity with the data consistency.

2.2.4. Numerical algorithm

To solve the problem in Eq. (8), we use the variable splitting and quadratic penalty technique proposed in (Yang et al., 2009) because of its advantage in handling the ℓ_1 norm-based optimization with image patches (Chen et al., 2010; Qu et al., 2012).

Base on the original algorithm, we rewrite Eq. (8) as

$$\min_{\mathbf{x},\boldsymbol{\alpha}} \sum_{j=1}^{J}\|\boldsymbol{\alpha}_j\|_1 + \frac{\lambda}{2}\|\mathbf{y}-\mathbf{F}_{\mathbf{U}}\mathbf{x}\|_2^2 \ s.t. \ \boldsymbol{\alpha}_j = \mathbf{A}_j\mathbf{x} \ \left(j=1,2,\cdots,J\right). \tag{9}$$

A relaxed unconstraint form of Eq. (9) is written as

$$\min_{\mathbf{x},\boldsymbol{\alpha}} \sum_{j=1}^{J}\left(\|\boldsymbol{\alpha}_j\|_1 + \frac{\beta}{2}\|\boldsymbol{\alpha}_j - \mathbf{A}_j\mathbf{x}\|_2^2\right) + \frac{\lambda}{2}\|\mathbf{y}-\mathbf{F}_{\mathbf{U}}\mathbf{x}\|_2^2. \tag{10}$$

The solution of Eq. (10) approaches that of (9) as $\beta \to \infty$ [7]. For practical implementation, with β gradually increasing, we use the previous solution as a 'warm start' for the next alternating optimization.

When β is fixed, Eq. (10) can be solved in an alternating fashion as follows:

For a fixed $\mathbf{x}$, solve

$$\hat{\boldsymbol{\alpha}}_j = \arg\min_{\boldsymbol{\alpha}_j} \ \|\boldsymbol{\alpha}_j\|_1 + \frac{\beta}{2}\|\boldsymbol{\alpha}_j - \mathbf{A}_j\mathbf{x}\|_2^2, \tag{11}$$

whose solution is obtained via soft thresholding for each $\boldsymbol{\alpha}_j$

$$\hat{\boldsymbol{\alpha}}_j = S\left(\mathbf{A}_j\mathbf{x}, \frac{1}{\beta}\right) = \max\left(|\mathbf{A}_j\mathbf{x}| - \frac{1}{\beta}, 0\right)\frac{\mathbf{A}_j\mathbf{x}}{|\mathbf{A}_j\mathbf{x}|}. \tag{12}$$

For fixed $\boldsymbol{\alpha}_j \left(j=1,2,\cdots,J\right)$, solve

$$\hat{\mathbf{x}} = \arg\min_{\mathbf{x}} \ \sum_{j=1}^{J}\left(\frac{\beta}{2}\|\boldsymbol{\alpha}_j - \mathbf{A}_j\mathbf{x}\|_2^2\right) + \frac{\lambda}{2}\|\mathbf{y}-\mathbf{F}_{\mathbf{U}}\mathbf{x}\|_2^2. \tag{13}$$

The minimizer of Eq. (13) is given by the solution of the normal equation

$$\left(\beta\sum_{j=1}^{J}\mathbf{A}_j^T\mathbf{A}_j + \lambda\mathbf{F}_{\mathbf{U}}^H\mathbf{F}_{\mathbf{U}}\right)\mathbf{x} = \beta\sum_{j=1}^{J}\mathbf{A}_j^T\boldsymbol{\alpha}_j + \lambda\mathbf{F}_{\mathbf{U}}^H\mathbf{y} \tag{14}$$

which can be simplified as

$$\beta\mathbf{O}\mathbf{x} + \lambda\mathbf{F}_{\mathbf{U}}^H\mathbf{F}_{\mathbf{U}}\mathbf{x} = \beta\mathbf{v}_{\boldsymbol{\alpha}} + \lambda\mathbf{F}_{\mathbf{U}}^H\mathbf{y}. \tag{15}$$

by incoporating Eq.(5) and the term

$$\mathbf{v}_{\boldsymbol{\alpha}} = \sum_{j=1}^{J}\mathbf{A}_j^T\boldsymbol{\alpha}_j \tag{16}$$

is an assembled image reconstructed from patches in all group. We use the linear conjugate gradient method to solve Eq. (15) (Shewchuk, 1994).

Overall, increasing β is accomplished in the outer loop of the iterative algorithm which will be terminated when β is sufficiently large. For a fixed β, Eq. (10) is solved in the inner loop which will be terminated when the increment of $\mathbf{x}$ is smaller than a given tolerance η. The algorithm is summarized in **Algorithm 1**. The proof of the convergence of the algorithm is similar to the one given in (Wang et al., 2008) with slight modifications, and thus is omitted here.

Algorithm 1. MRI reconstruction via patch-based nonlocal operator (PANO) with fixed similarity relationship

Initialization: Input the PANO $\mathbf{A}_j\left(j=1,\cdots,J\right)$, acquired k-space data $\mathbf{y}$, diagonal matrix $\mathbf{O}$ and the fast operator $\mathbf{F}_{\mathbf{U}}$, regularization weight λ and tolerance of inner loop $\eta = 5\times10^{-3}$. Initialize $\mathbf{x} = \mathbf{F}_{\mathbf{U}}^{H}\mathbf{y}$, $\mathbf{x}_{\text{last}} = \mathbf{x}$, $\beta = 2^6, \beta_{\max} = 2^{12}$, and $\boldsymbol{\alpha}_j = \mathbf{0}$ for all $j=1,2,\cdots,J$

Main:

While $\beta \le \beta_{\max}$

    1. For $j=1$ to J, given $\mathbf{x}$, solve Eq. (12);

    2. Update the assembled image $\mathbf{v}_{\boldsymbol{\alpha}}$ using Eq. (16);

    3. Solve Eq. (15) with linear conjugate gradient method and the solution is $\mathbf{x}$;

    4. If $\left\|\Delta\mathbf{x}\right\| = \dfrac{\left\|\mathbf{x}_{\text{last}} - \mathbf{x}\right\|}{\left\|\mathbf{x}_{\text{last}}\right\|} > \eta$, $\mathbf{x}_{\text{last}} \leftarrow \mathbf{x}$, go to step 1; Otherwise, go to step 5;

    5. $\hat{\mathbf{x}} \leftarrow \mathbf{x}_{\text{last}}, \beta \leftarrow 2\beta$, go to step 1.

Otherwise **End While**

Output: $\hat{\mathbf{x}}$

2.2.5. Learn the nonlocal similarity from undersampled data

In the sections above, we assume that the nonlocal similarity is learnt from an available fully sampled image. In this section, we will discuss how to obtain a proper guide image to learn the nonlocal similarity from undersampled data. It is interesting to note that the concept of using guide images has been previously used in medical image superresolution problems (Manjon et al., 2010; Rousseau, 2010).

We consider estimating the nonlocal similarity from a guide image reconstructed from:

1) Low-frequency k-space measurements;

2) Zero-filling k-space by filling zeros into the un-sampled k-space;

3) Conventional CS-MRI method.

The 1st scheme is adopted in (Akçakaya et al., 2011) and only utilizes the low-resolution image (Fig. 3(d)) assuming that low-frequency k-space data are sufficient to approximately represent the similarity relationship. The 2nd and 3rd schemes explore all the acquired k-space data. The 2nd scheme results in obvious artifacts in the guide image (Fig. 3(e)) and the 3rd scheme depends on good CS reconstruction method to remove the artifacts (Fig. 3(f)). In the 3rd scheme, the shift-invariant discrete wavelet transform (SIDWT) (Baraniuk et al., 2009) is utilized with variable splitting and quadratic penalty technique (Yang et al., 2009) to reconstruct the guide image. We choose SIDWT because it can mitigate blocky artifacts introduced by orthogonal discrete wavelet transform (Baker et al., 2011; Hu et al., 2011). SIDWT in (Baraniuk et al., 2009)

is adopted for its efficient implementation. How these guide images affect the reconstruction will be analyzed in the section 3.1.
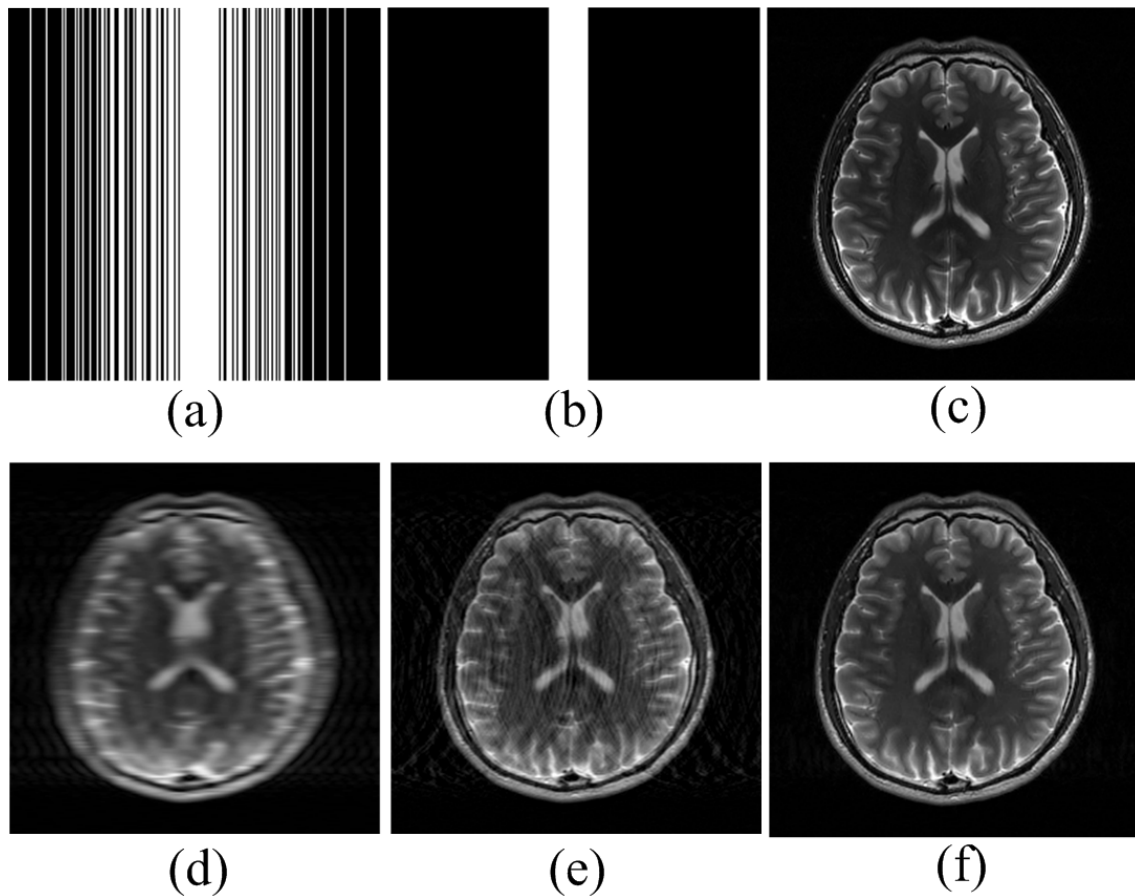

Fig.3. Comparison of different guide images. (a) variable density Cartesian sampling pattern with sampling rate 0.40; (b) locations of low-frequency k-space data; (c) the fully sampled MR image; (d) reconstructed image from only the low-frequency k-space data; (e) reconstructed image from zero-filled k-space data; (f) reconstructed image from SIDWT.

Once the guide image is reconstructed, it is utilized to learn the patch similarity assuming this guide image appropriately represents the similarity of nonlocal patches. The similarity information guides the design of PANO to achieve the sparse vectors of grouped similar patches. Then, image $\mathbf{x}$ is reconstructed by regularizing the ℓ_1 norm of the sparse vectors. The proposed scheme is shown in Fig. 4.
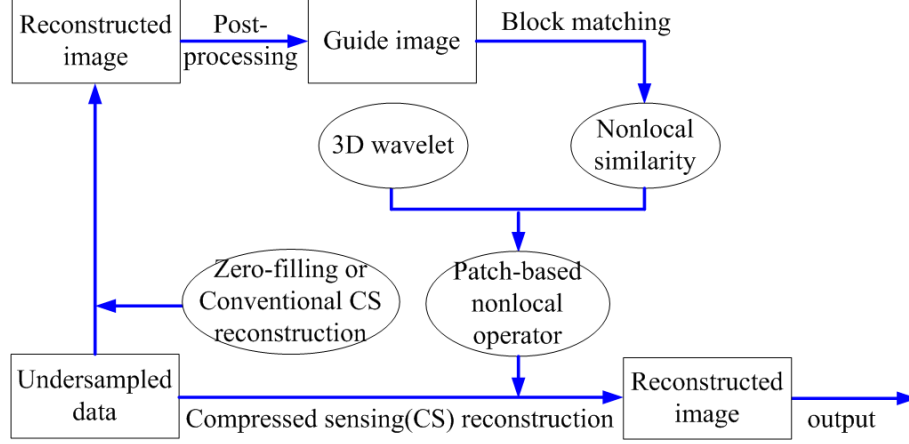
Fig.4. Flowchart of the proposed PANO-based MRI reconstruction from undersampled data.

If the PANO-based reconstruction can improve the reconstruction, one may consider further learning the similarity from the subsequent reconstruction. An improved algorithm with the updated guide image is shown in **Algorithm 2**.

Details on how guide images affect the final reconstruction are discussed in Section 3.1.

Algorithm 2. PANO-based MR reconstruction with updated guide images

---

Initialization: Set the times of updating the guide image as $Q = 2$. Input the acquired k-space data $\mathbf{y}$, the fast operator $\mathbf{F_U}$, 3D fast Haar wavelet operator $\mathbf{\Psi}_{3D}$, regularization weight λ and the tolerance of inner loop $\eta = 5 \times 10^{-3}$. Initialize $\mathbf{x} = \mathbf{F_U}^H \mathbf{y}$, $\mathbf{x}_{\text{last}} = \mathbf{x}$, $\beta = 2^6$, $\boldsymbol{\alpha}_j = \mathbf{0}$ for all $j = 1, 2, \cdots, J$, and $q = 1$.

Main:

1. Obtain the 1st guide image $\mathbf{x}_1$ by solving Eq. (2) with SIDWT as the sparsifying transform;

For $q = 1, \cdots, Q$

2. Estimate $\mathbf{R}_{v_j} (j = 1, 2, \cdots, J)$ from q^{th} guide image according to Eq. (7);

3. Update the diagonal matrix $\mathbf{O} = \sum_{j}^{J} \mathbf{A}_j^T \mathbf{A}_j$;

4. Reconstruct $\hat{\mathbf{x}}$ using Algorithm in 1 with updated $\mathbf{R}_{v_j} (j = 1, 2, \cdots, J)$ and $\mathbf{O}$;

5. Update reconstructed image $\hat{\mathbf{x}}_q \leftarrow \hat{\mathbf{x}}$ and the guide image $\mathbf{x}_{q+1}$;

6. Update $q \leftarrow q + 1$

End For

Output: $\hat{\mathbf{x}}_Q$

---

3. Results

To evaluate the performance of the proposed method, how the guide image affects the final reconstruction will be analyzed first. Then, the performance of the proposed method is demonstrated with experimental data at various undersampling factors. Sparsity-based image reconstruction using two typical sparsifying transforms, total variation (TV) (Block et al., 2007; Haldar et al., 2011; Lustig et al., 2007) and SIDWT, are compared with the proposed PANO-based image reconstruction method. All these methods are implemented with variable splitting and quadratic penalty technique (Yang et al., 2009). Default parameters of the algorithm are shown in **Algorithm 1**. The Daubechies wavelet with 4 decomposition levels is utilized for SIDWT. For the proposed method, the similar blocks are found from the magnitude of image. Empirically, learning similarity from magnitude image performs slightly better than separately learning from imaginary and real parts.

To evaluate the reconstruction error, we use the relative ℓ_2 norm error (RLNE) defined as

$$e(\hat{\mathbf{x}}) = \frac{\|\hat{\mathbf{x}} - \tilde{\mathbf{x}}\|_2}{\|\tilde{\mathbf{x}}\|_2} \tag{17}$$

to measure the difference of reconstructed image $\hat{\mathbf{x}}$ and fully sampled image $\tilde{\mathbf{x}}$.

The fully sampled complex MR image (size 256×256), as shown in Fig. 2(c), is acquired from a healthy volunteer at a 3T Siemens Trio Tim MRI scanner using the T2-weighted turbo spin echo sequence (TR/TE=6100/99 ms, 220×220 mm field of view, 3 mm slice thickness). We do the SENSE reconstruction with reduction factor 1 to compose full k-space of gold standard images. These full k-space data will be used for emulate single-channel MRI.

The signal-to-noise ratio (SNR) of this data is 33, which is measured on the magnitude image according to

$$\text{SNR} = \frac{\mu}{\delta}, \tag{18}$$

where μ is the mean of image and δ is the standard deviation of noise extracted from the background of image (Dietrich et al., 2007; Henkelman, 1985; Qu et al., 2012).

3.1. Effects of the guide image

The sampling pattern with the gradually varying sampling density from the k-space center outwards is shown in Fig. 3(a).

With the fully sampled image as the guide image, one can learn the best similarity. By integrating this similarity information into PANO, a high quality reconstruction, shown in Fig. 5(a), is obtained from undersampled data.

When only the undersampled data is available and only learning the similarity from guide image for one time, some artifacts are observed in the reconstructed images with the guide
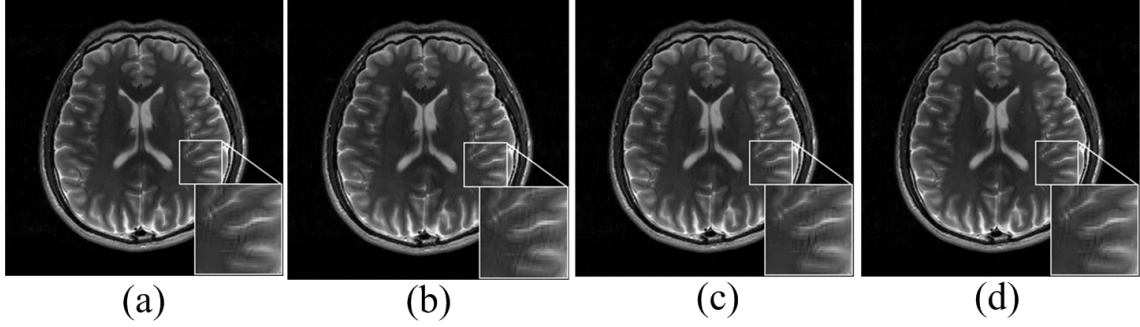
Fig.5. Images reconstructed using proposed method with the different guide images (a) fully sampled image in Fig. 3(c), (b) low-resolution image in Fig. 3(d), (c) zero-filling image in Fig. 3(e), and (d) conventional CS-MRI reconstruction in Fig. 3(f). The RLNEs of (a)-(d) are 0.077, 0.087, 0.083, 0.081.

images from the low-resolution image. Using zero-filling image or SIDWT-based reconstruction as the guide image, the aliasing artifacts are less.

For different initial guide images, very similar reconstruction error, shown in Fig. 6(a), are obtained by iteratively learning the similarity from PANO-based reconstructed images. This is mainly because of the properly reconstructed image using PANO although some strong artifacts are existed in the initial guide image in Figs. 3(d) and (e). By further learning similarity from images in Fig. 5, very similar reconstructed images are achieved which are not shown to save pages. This implies that the iterative learning similarity in the proposed method is not sensitive to the initial guide image. The same observation are found for lower sampling rate in Fig. 6(b) and another sampling pattern in Fig. 6(c) where the sampled low-frequency k-space data are 25% of all the sampled phase encodings while the rest sampled k-space data are randomly selected. Testing on other image slices acquired on the same volunteer using same pulse sequence are consistent to the observation here.

We suggest adopting the zero-filling image as guide image since it makes use of all the sampled data and does not require extra computation except one time fast Fourier transform.
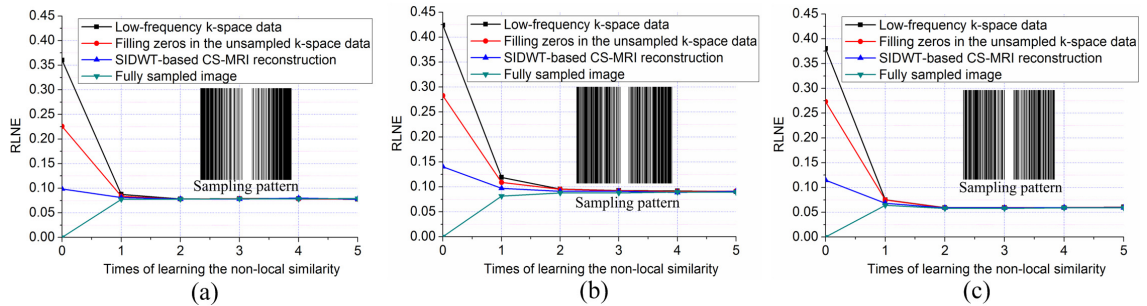

Fig.6. Reconstruction error of the PANO method with updated guide images. Note: The "0" in the axis means the RLNE between the guide image and the fully sampled image. (a) and (b) are RLNE curves for the undersampled simulated data with sampling rate 0.40 and 0.28, respectively; (c) is the RLNE cure for a sampling pattern where more sampled data are sampled in high-frequency k-space with sampling rate 0.40.

3.2. Comparison with conventional CS-MRI methods

The variable density sampling pattern, shown in Fig. 7(a), is utilized to undersample the k-space data. λ is set as 10^6 for PANO, SIDWT and TV. All the reconstruction problems are numerically solved using the variable splitting and quadratic penalty technique (Yang et al., 2009).

Only with the undersampled data, the conventional CS-MRI with SIDWT or TV leads to obvious artifacts shown in Figs. 7(c) and (d). The proposed PANO-based method preserves the fine edges and does not introduce obvious artifacts as shown in Fig. 7(e). Visual inspection is consistent with the reconstruction error evaluation shown in Fig. 8. The proposed method reduces the reconstruction error of traditional CS-MRI methods nearly by 30% and produces the lowest RLNE among all the three reconstruction methods.
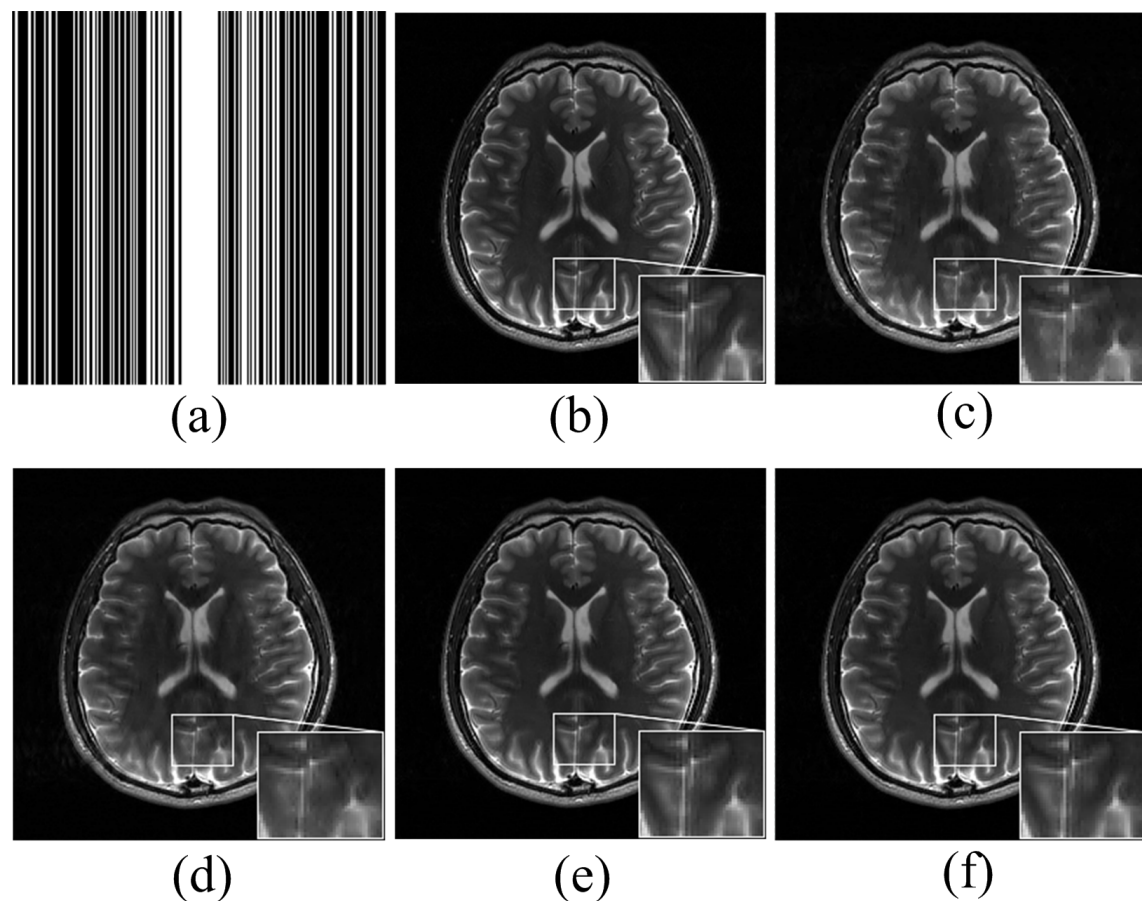
Fig.7. Comparison of reconstructions from different methods (SNR=33). (a) The Cartesian sampling pattern with sampling rate 0.40; (b) fully sampled image; (c) reconstructed image using TV, the RLNE=0.111; (d) reconstructed image using SIDWT, the RLNE=0.114; (e) reconstructed image using PANO (guide image reconstructed from incomplete data), the RLNE= 0.059; (f) reconstructed image using PANO (guide image reconstructed from fully sampled data), the RLNE= 0.057.

The reconstruction of the proposed method with similarity learnt from undersampled data is very close to that using the proposed method with the similarity extracted from the fully sampled data (shown in Figs. 7(e) and (f)). The error is nearly the same when the sampling rate is relatively high (greater than 0.35 as shown in Fig. 8). This implies that if the sampling rate is relatively high, our method may fully take advantage of the nonlocal similarity of the unknown image.

When the k-space data are highly sampled (lower than 25%), the reconstructed images with similarity learnt from undersampled data is sub-optimal comparing with those with similarity leant from fully sampled data. This leaves the chance to incorporate other prior information to help image reconstruction that will be described in Section 3.3.
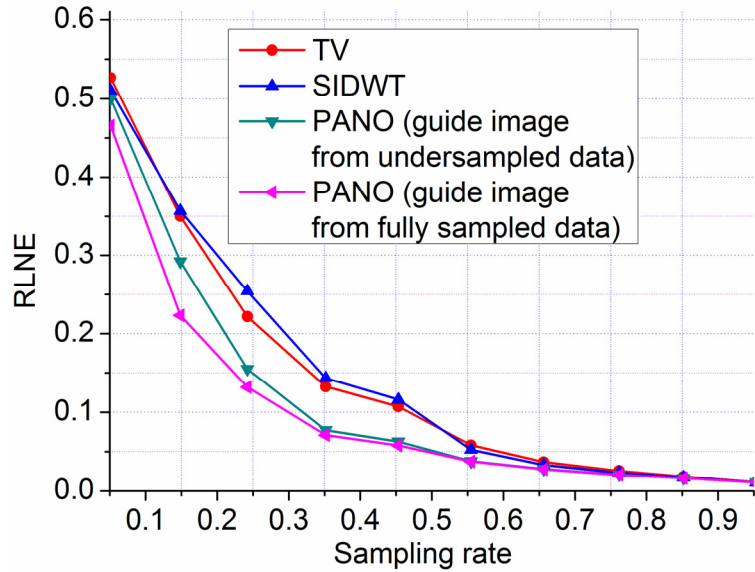
Fig.8. The reconstruction error versus sampling rate.

3.3. Image reconstruction with similarity learnt from multi-contrast images

In MRI experiments, multi-contrast images may be acquired. For example, T1 and T2 weighted images are usually used in clinical diagnosis. Sometimes anatomical information is shared in these contrast images as shown in Figs. 9(a) and (c). It is possible to learn semilarities from one contrast image and incorporate this information into another contrast image reconstruction. When T2 weighted image is undersampled at sampling rate 0.25, PANO fails to reconstruct the edges as shown in Fig. 9(c). By learning the similarity from the fully sampled T2 weighted image, edges are reconstructed much clearer.
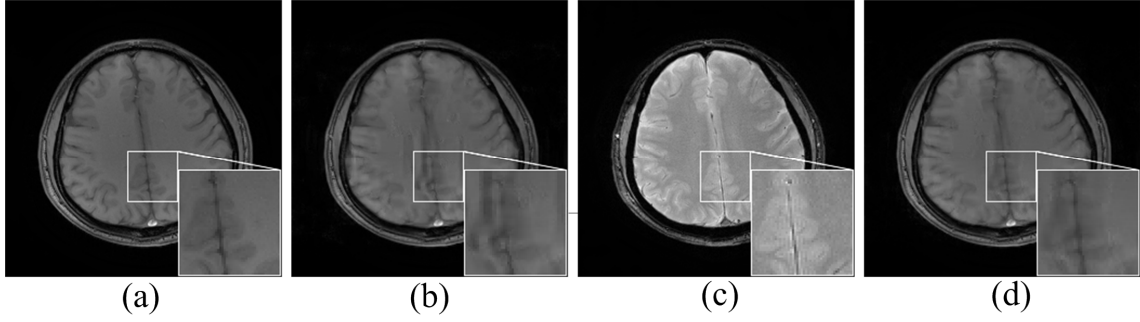
Fig.9. Reconstructed images by learning similarities from another contrast image. (a) fully sampled image T2-weighted image; (b) reconstructed image using PANO (guide image reconstructed from 25% T2-weighted image data), the RLNE=0.109; (c) fully sampled T1-weighted image; (d) reconstructed image using PANO (guide image reconstructed from 100% T1-weighted image data), the RLNE=0.070. Note: The complex images in (a) and (c) are acquired from a healthy volunteer at a 1.5T Philips MRI scanner with sequence parameters (T1-weighted image: TR/TE=1700/390 ms, T2-weighted image: TR/TE= 3000/800ms, both images are with 230×230 mm field of view, 5 mm slice thickness).

4. Discussion

4.1. Sampling patterns

To test the performance of PANO with different sampling patterns, the pseudo radial sampling (Chen et al., 2010; Qu et al., 2010b; Trzasko and Manduca, 2009), shown in Fig. 9(a) and 2D random sampling (Lustig et al., 2007; Qu et al., 2010b; Ravishankar and Bresler, 2011), shown in Fig. 10(b), are used to undersample the k-space data of Fig. 3(c). Reconstruction errors shown in Figs. 10(a) and (b) indicate that the proposed algorithm consistently outperforms the conventional CS-MRI methods when the sampling rate is smaller than 0.4. This implies that the proposed method can consistently improve the reconstruction of traditional wavelet-based or TV-based reconstruction for a larger class of sampling patterns.
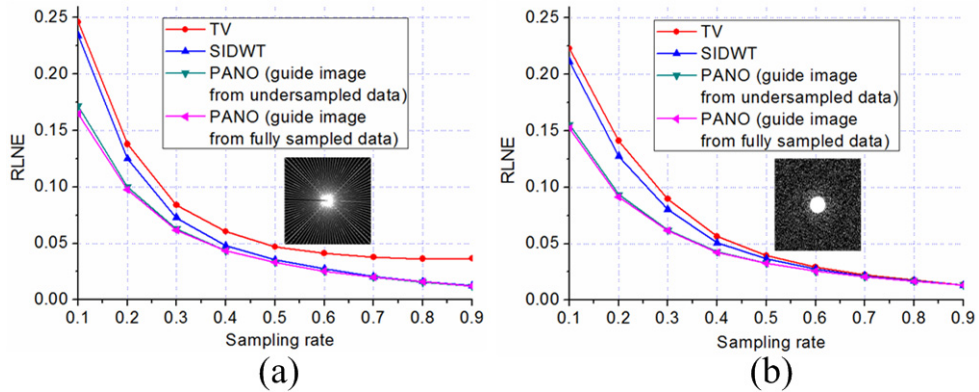

Fig.10. The RLNEs versus sampling rates for Fig. 7(b) (SNR=33). (a) and (b) are RLNE curves for the psudo radial and 2D random sampling patterns, respectively. Note: For the 2D random sampling pattern, the central region corresponds to 12.5% of all the sampled data.

For the same sampling rate, two type of varying sampling density shown in Figs. 3(a) and 7(b) are analyzed in Fig. 11. Comparisons on Fig. 11(a) with Fig.11 (b), and Fig. 11(c) with Fig. 11 (d), imply that the gradually varying sampling density (Fig. 3(a)) will reduce the overall reconstruction error for SDIWT but it leads to loss of edge structures for both SIDWT and PANO. SIDWT with sampling pattern of more high-frequency data (Fig. 7(b)) obtains sharper edges in Fig. 11(b) but it introduces aliasing artifacts in the smooth region. These artifacts are removed using PANO as shown in Fig. 11(d). One explanation for this is that PANO may sparser represent the low-dimensional structures (Akçakaya et al., 2011), e.g. smooth region, than conventional sparsifying transform. Therefore, for a given sampling rate, assigning more high-frequency data for PANO will improve the reconstruction of edges but the aliasing artifact in the smooth region is still suppressed. For each sampling pattern, PANO preserves the edges better than SIDWT by comparing Fig. 11(b) with Fig. 11 (c), and Fig. 11(b) with Fig. 11 (d). Overall, PANO outperforms SIDWT in terms of preserving the edge and lower reconstruction error.
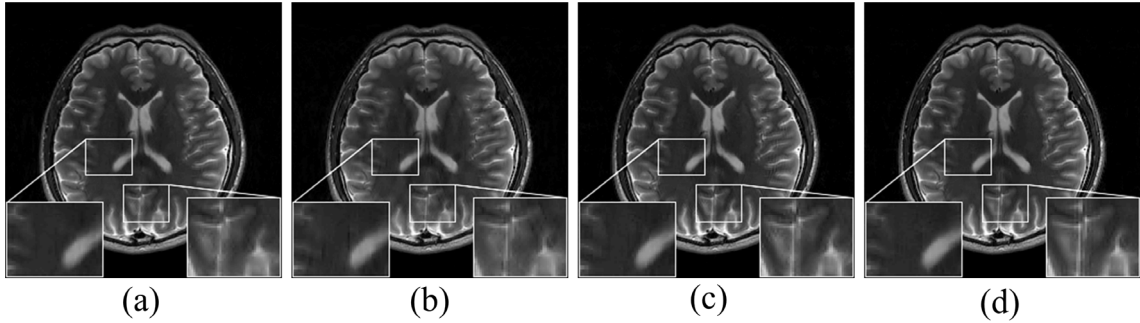

(a) (b) (c) (d)

Fig.11. Comparisons on variable density sampling pattern at sampling rate 0.40. (a) and (b) are reconstructed images using SIDWT with the sampling patterns in Fig. 3(a) and Fig. 7(a) respectively, (c) and (d) are reconstructed images using PANO with the sampling pattern in Fig. 3(a) and Fig. 7(a) respectively. The RLNEs of (a)-(d) are 0.098, 0.114, 0.077, and 0.059.

In paractice, the pseudo radial and 2D random sampling patterns could be useful for 3D imaging where 2D phase encodings are available and 2D undersampling are applicable. For example, Cartesian sampling with CAPR (Cartesian Acquisition with Projection-Reconstruction-like) may be constructed and tends to exhibit properties similar to non-Cartesian radial trajectories in 3D imaging (Trzasko et al., 2011). In 2D imaging, radial (Block et al., 2007; Knoll et al., 2011) or spiral trajectories (Seeger et al., 2010) can be used to undersample k-space data. They are more realistic to accelerate imaging than 1D random sampling. However, regridding in non-uniform FFT for spiral or radial may affect the grouping of similar patches thus PANO should be applied carefully.

4.2. Reconstruction on more brain images

In this section, we will demostrate the proposed method works better than convenitonal

CS-MRI for T2-weighted brain image. Four images, shown in Fig.12, acquired with the same pulse sequences on 3T Siemens Trio Tim MRI scanner. We do the SENSE reconstruction with reduction factor 1 to compose full k-space of gold standard images. The sampling pattern shown in Fig. 7(a) with 40% k-space data are used for reconstruction. Reconstruction error shown in **Table 1** implies that PANO always performs better than SIDWT and TV does. Due to the limited access to the k-space data, only T2-weighted brain images are analyzed. Verification of the proposed method on more datasets is worthy further investigation.

| (a) | (b) | (c) | (d) |
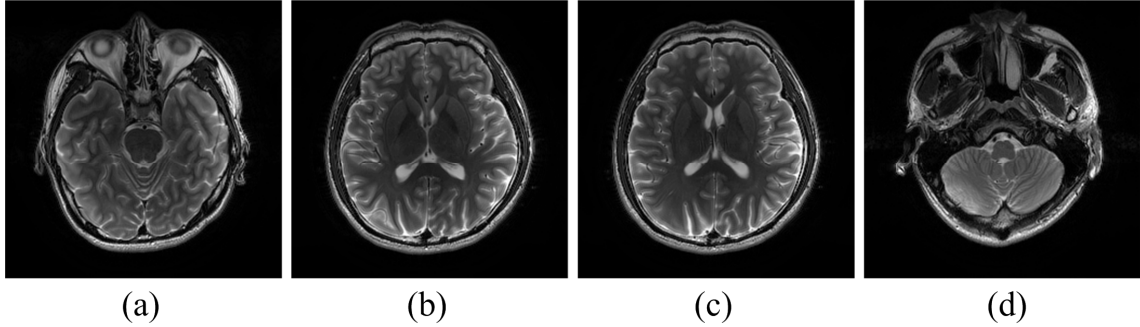
Fig.12. Four T2-weighted images.

Table 1. The Reconstruction error RLNEs for other four images.

Images	Reconstruction methods		
	TV	SIDWT	PANO
Fig.12(a)	0.121	0.120	0.085
Fig.12(b)	0.113	0.113	0.074
Fig.12(c)	0.109	0.111	0.069
Fig.12(d)	0.113	0.116	0.095

4.3. Sampled data with more noise

To demonstrate the ability of the proposed method in handling noise, Gaussian white noise with standard deviation 0.015 was added to both the real and the imaginary parts of the original k-space data. The SNR is changed to 10. We specify the regularization parameters be $\lambda = 3 \times 10^2$ for TV-based reconstruction, $\lambda = 2 \times 10^2$ for SIDWT-based reconstruction, and $\lambda = 10^3$ for the proposed methods. In simulation, regularization parameters of different methods are manually optimized to achieve the minimum RLNEs and remove most of the noise by maintaining SNR≥15 in the reconstructed images. Empirically, the adaptive 3×3 Wiener filtering is helpful and utilized to remove the artifacts and noise from the guide image in the proposed method.

Obvious artifacts in the reconstructed images are observed for TV-based, and SIDWT-based CS-MRI methods (shown in Figs. 13(c)-(d)), while the proposed method preserves the edges of the reconstructed image (shown in Fig. 13(e)).

By incorporating a TV constraint $\mathrm{TV}(\mathbf{x})$ into the PANO reconstruction as

$$\hat{\mathbf{x}} = \arg\min_{\mathbf{x}} \sum_{j=1}^{J} \|\mathbf{A}_j \mathbf{x}\|_1 + \gamma \mathrm{TV}(\mathbf{x}) + \frac{\lambda}{2} \|\mathbf{y} - \mathbf{F}_U \mathbf{x}\|_2^2, \qquad (19)$$

where γ trades PANO sparsity with finite-differences sparsity, and setting $\gamma = 1$ and $\lambda = 10^3$, the noise is further reduced in the reconstructed images comparing Fig. 13(e) with Fig. 13(f). The SNR is increased from 22.47 and 28.00. This implies that TV is helpful for PANO to remove the noise.
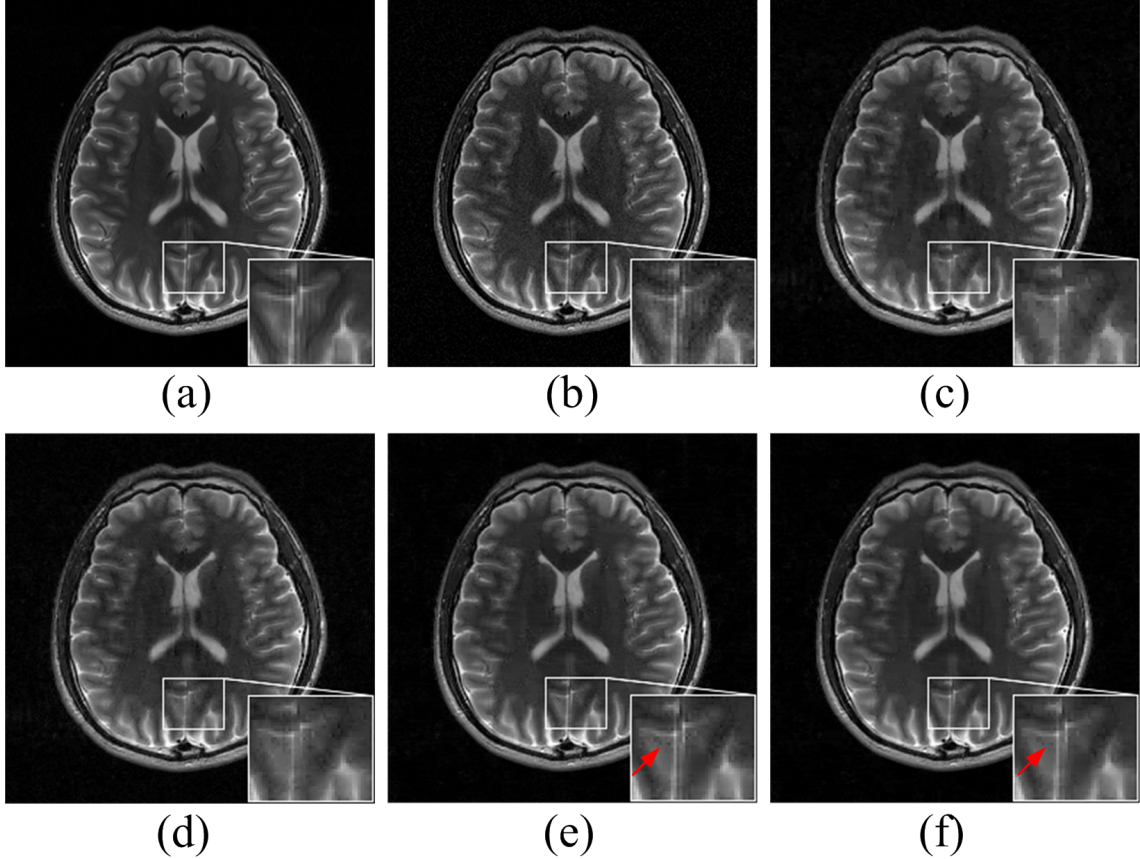
Fig.13. Reconstructed images from noise-added k-space data (SNR=9.60) with variable density Cartesian sampling pattern at sampling rate 45%. (a) reconstructed image from fully sampled data (SNR=33), (b) reconstructed image from fully sampled data with added noise (SNR=9.60), (c)-(f) are reconstructed images from undersampled data using TV, SIDWT, PANO, and PANO+TV respectively. The RLNEs of (c)-(f) are 0.129, 0.124, 0.099 and 0.100, respectively. The SNRs of (d)-(g) are 16.0, 16.40, 22.47 and 28.00, respectively.

4.4. Parameters in PANO

Additional parameters of PANO include the number of similar patches (Q), patch size (L), and the size of search range (D). How these parameters affect the reconstruction will be analyzed in this section.

Increasing Q will reduce the reconstruction error and will not significantly change the error when $Q \geq 8$ as shown in Fig. 14(a). $Q = 8$ is suggested since the computation complexity of

one forward/backward PANO is proportional to Q.

Increasing L will increase the reconstruction error and $L = 8$ is suggested. But the change of RLNE is relatively small (smaller than 0.01) when the patch size is relative small ($L \leq 16$ for the image size 256×256). This is shown in Fig. 14(b). Too large patch size ($L \geq 32$ for the image size 256×256) will increase the reconstruction error. One reason may be similarity between the two large size patches is not obvious than that of small size patches, which results in the sparsity is not sufficient for image reconstruction.

Different D will achieve very close reconstruction error as shown in Fig. 14(c). This implies that the proposed method is not sensitive to the search range. The reconstruction error slightly increases (change of RLNE is smaller than 0.005) when D is large ($D \geq 80$ for the image 256×256). Ideally, if the fully sampled image is available to serve as guide image, the reconstruction error nearly does not change by increasing as shown in Fig. 14(c). This implies too large ($D \geq 80$ in our case) search arrange does not mean better reconstruction for the undersampled MRI reconstruction if D is large enough. One reason for the slightly increased reconstruction error may be that searching the similar patches is not exactly right for the guide image reconstructed from undersampled data. Therefore, $15 \leq D \leq 80$ is suggested.

Since the Q similar patches are re-ordered into 3D array according to sorted ℓ_2 norm distance between the reference patch and similar patches, it is meaningful to analyze how this reordering can affect the reconstruction. The proposed PANO-based method is not sensitive to the re-ordering as demonstrated in Fig. 14(d). For the 8 similar patches, the order of partial patches in each 3D array is randomly permutated. The reconstruction error only slightly increase (smaller than 0.005) when the order of all the patches in are permutated within each 3D array.
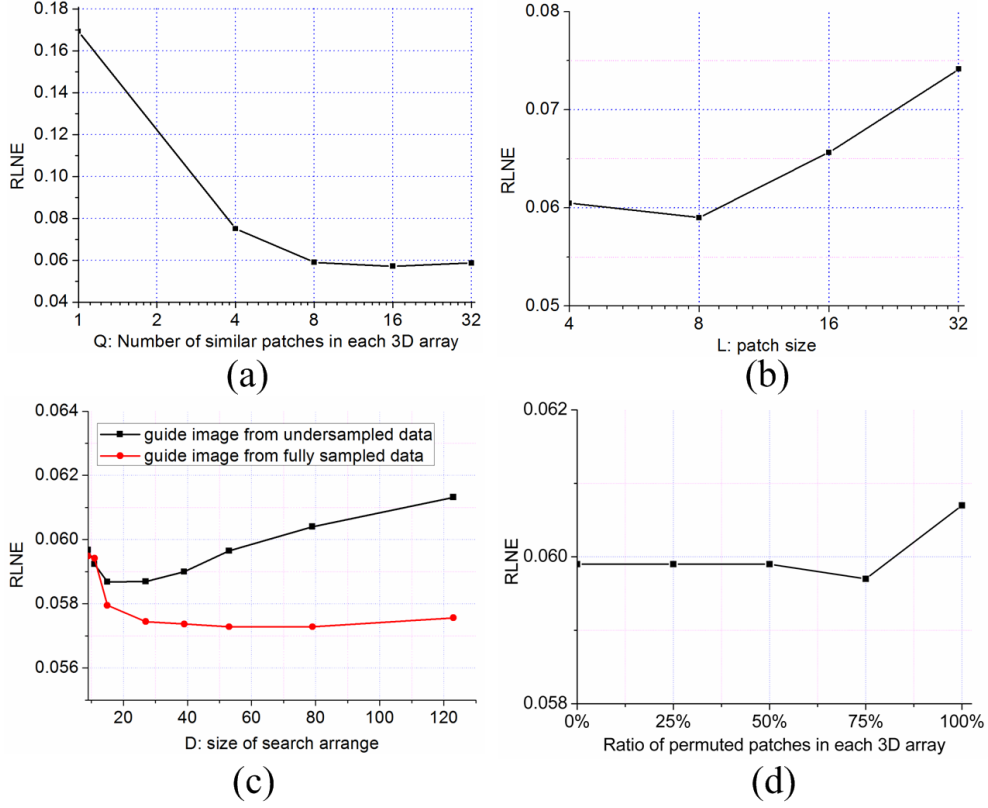
Fig.14. The RLNEs of PANO versus the parameters. (a) Q (number of similar patches in each 3D array) when $L=8$ and $D=39$, (b) L (patch size) in PANO when $Q=8$ and $D=39$, (c) D (size of search range) when $L=8$ and $Q=8$, and (d) the ratio of permuted patches in each 3D array in PANO when $L=8, Q=8$ and $D=39$.

4.5. Regularization parameters

The regularization parameter λ trades the sparsity and data consistency. Generally, the regularization parameter can be selected using the L-curve method by plotting the sparsity term against the fidelity term (Adluru and DiBella, 2008; Wu et al., 2011). However, L-curve method requires implementing the reconstruction more than one time, thus it is time consuming. One can also try the robustness choice of parameters by incorporating the adaptive regularization derived from maximum likelihood estimate (Chen et al., 2010). Another choice is to set the regularization parameter corresponding to the lowest threshold for a blindly estimate the noise level (Hu et al., 2011).

The data we used in this paper is with high SNR, thus the regularization parameter λ can be largely enough ($\lambda=10^6$ in our case). We observed that $\lambda>10^6$ will not obviously change the reconstructed image and the reconstruction error RLNE. For the manually added noise, λ is chosen carefully to achieve the lowest RLNE and remove most noise by maintaining $\mathrm{SNR} \geqq 15$. Design a robustness regularization parameter will be our future work.

4.6. Comparision with other CS-MRI reconstruction methods

In this section, we compare the proposed method with some previously proposed CS-based reconstruction methods. These methods include Lustig's method (Lustig et al., 2007), Yang's method (Yang et al., 2010), Chen's method (Chen and Huang, 2012) , Huang's method (Huang and Yang, 2012) and Egiazarian's method (Egiazarian et al., 2007), repectively. Egiazarian's method adopts recursive spatially adaptive filtering to reconstruction 2D image and its extenstion into 3D image reconstruction is in (Maggioni et al., 2013).

Results in Fig.15 imply that Chen's method (Fig. 15(d)), enforcing wavelet tree sparsity, outperforms Lustig's (Fig. 15(b)) and Yang's (Fig. 15(c)) methods in terms of lower reconstruction errors. Huang's method (Fig. 15(d)) further improves the reconstructed edges by incorporating nonlocal total variation. Edges are preserved well using Egiazarian's method (Fig. 15(e)) by making use of non-local patch based redundancy but obvious artifacts are observed in the smooth region. The proposed method outperforms these methods in term of visual quality and reconstruction errors. The lowest reconstruction errors, listed in **Table 2**, imply that the superior performance of the proposed method still holds for other tested images. In summary, the proposed method outperforms other methods in term of better image quality and lower reconstruction errors.
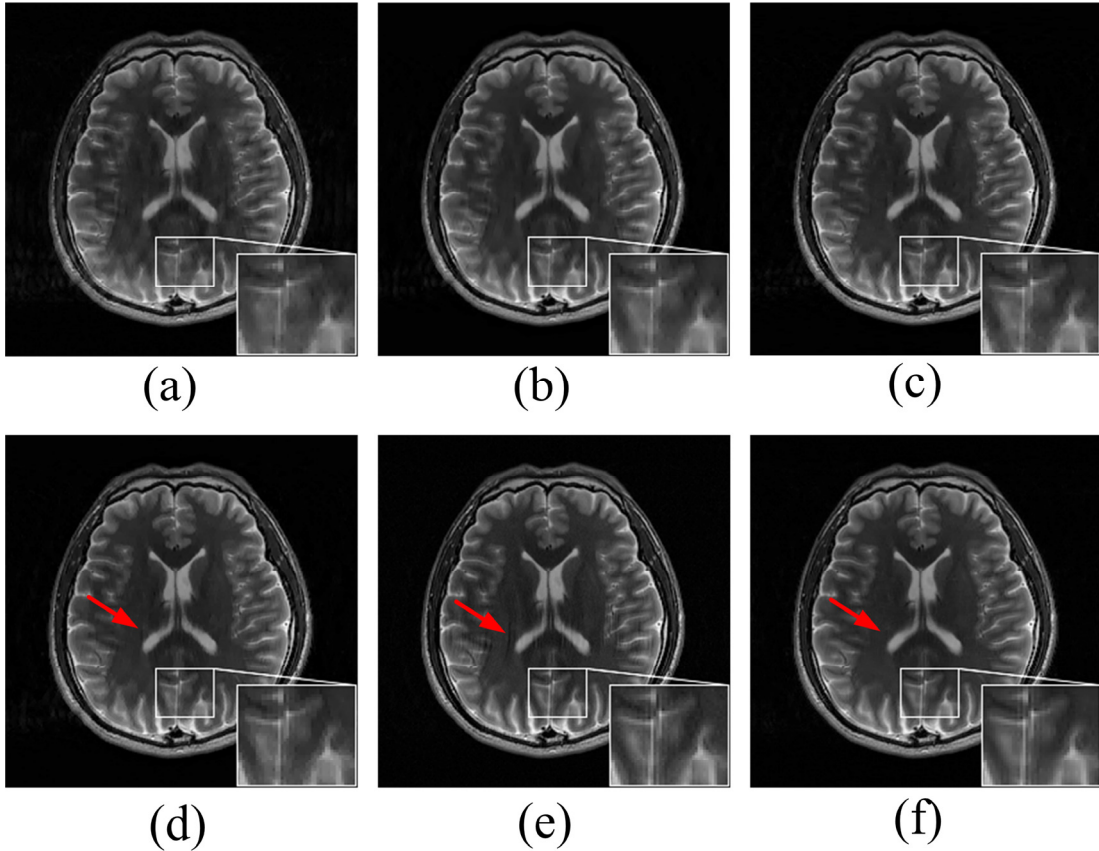

Fig. 15. Reconstructed images using other CS-MRI methods and PANO when 40% data are sampled. (a) is the fully sampled image, (a)-(f) are reconstructed images using Lustig's, Yang's, Chen's, Huang's, Egiazarian's and the proposed method. RLNEs of (a)-(d) are 0.140, 0.106, 0.091, 0.083, 0.093 and 0.060, respectively.

Table 2. RLNEs for other four images using other CS-MRI reconstruction methods.

Images	Reconstruction methods					
	Lustig's	Yang's	Chen's	Huang's	Egiazarian's	Proposed
Fig.12(a)	0.156	0.115	0.108	0.099	0.106	0.085
Fig.12(b)	0.156	0.122	0.111	0.104	0.104	0.074
Fig.12(c)	0.153	0.116	0.102	0.097	0.108	0.069
Fig.12(d)	0.149	0.130	0.126	0.120	0.147	0.095

4.7. Reordering patches versus reordering pixels

Re-ordering the pixels with a guide image to enhance the sparsity and improve reconstruction was previously investigated in undersampled MRI reconstruction (Adluru and DiBella, 2008; Wu et al., 2011). We name these methods as re-order pixels-based sparse reconstruction (RPSR). The key difference is our reordering is implemented among the most Q similar patches while RPSR reordering for all the pixels. The advantage of the patch-based re-ordering is that this method can attenuate the influence of the aliasing on the accuracy of the sorting, which results in PANO-based method is not sensitive to the re-ordering in undersampled MRI reconstruction, as shown in Fig. 14(d).

One simulation is conducted to compare the performance of RPSR with the proposed PANO. The RPSR is implemented according to literature (Adluru and DiBella, 2008). With the fully sampled image as guide image, both RPSR and PANO can reconstruct the MR image very well as shown in Fig. 16. RPSR preserves the image details better than PANO. However, fully sampled guide image is not available in practice. With a guide image estimated from undersampled data, RPSR does not remove some artifacts in the reconstruction but PANO can. This implies RPSR is more sensitive to the guide image than PANO.
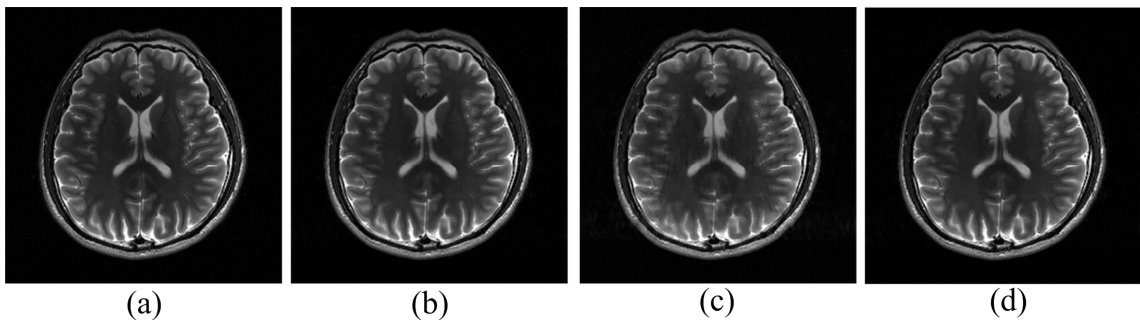

| (a) | (b) | (c) | (d) |

Fig.16. Comparison on the reconstructed image with RPSR and PANO methods. (a) and (b) are reconstructed images using RPSR and PANO methods with fully sampled image as guide image, (c) and (d) are reconstructed images using RPSR and PANO methods with TV-based undersampled k-space reconstruction as guide image. RLNEs of (a)-(d) are 0.028, 0.057, 0.114 and 0.059, respectively. Note: the sampling rate is 0.40 and the sampling pattern is shown in Fig. 6(a), the SNR of fully sampled image is 30. We tried several guide images from undersampled data for RPSR, and TV-based conventional CS-MRI reconstruction leads to the lowest reconstruction error in RPSR.

4.8. Reconstruction raw k-space data

To start with raw k-space data acquired from a real scanner, we undersample k-space data of each channel according to 1D random sampling pattern shown in Fig. 7(a). Then we reconstruct images channel-by-channel and compose the final image by performing some-of-square on these single-channel images. Fig. 17 shows that edges are preserved better and lower reconstruction errors are achieved using PANO than SIDWT and TV.
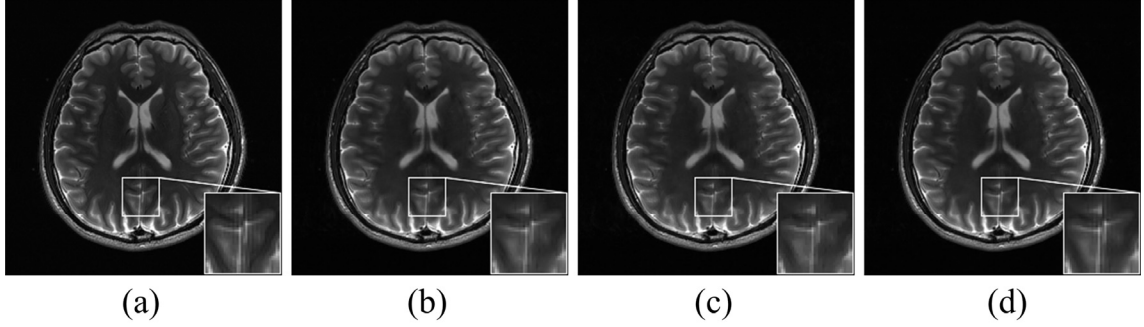

(a)　　　　　　　(b)　　　　　　　(c)　　　　　　　(d)

Fig.17. Reconstructed images using raw k-space data of each channel acquired from a real scanner. (a) Some-of-square image reconstructed from each channel data with fully sampling, (b)–(d) are some-of-square images reconstructed from each channel data with 1D undersampling using TV, SIDWT and PANO, respectively. The reconstruction error RLNEs for (b)–(d) are 0.080, 0.073 and 0.062, respectively. Note: 40% data are sampled according to the sampling pattern in Fig. 7(a).

4.9. Computation time

The programs run on 8 Cores 3.4GHz CPU desktop computer with 8GB RAM. The process from the image patches to 3D Haar wavelet coefficients and the soft thresholding on wavelet coefficients are implemented with C++. Without considering the iterations in the numerical algorithm, the computational complexity of one forward/backward PANO is $O(NQ)$ where N is the number of total pixels in a 2D image and Q is the number of similar patches in each 3D array. We designed a multi-thread computation for the 3D wavelet transform on 3D cubes and soft thresholding in PANO. It accelerate the forward/backward PANO by a factor of 3 when 8 threads is applied on our platform. The total reconstruction time of the proposed method is 73 seconds, as shown in Table 3, which we believe is acceptable for many applications which do not require online reconstruction. We also expect to further speed up the reconstruction by using more advanced computing architectures such as general purpose graphics processing units (Zhuo et al., 2010).

Table 3. Computation time for different methods (units: seconds).

	The proposed method			TV	SIDWT
Initial guide image	1st PANO reconstruction	2nd PANO reconstruction	Total computation time		
Zero-filling image	42.3	30.5	72.8		
Low-frequency k-space data	41.5	30.6	72.1	11	7.6
SIDWT-based reconstruction	41.9	30.6	72.5		

Note: Computations were performed on 8 Cores 3.4GHz CPU desktop computer with 8GB RAM. 40% k-space data of Fig. 2(c) is reconstructed with parameters of PANO L=8, Q=8, and D=39.

5. Conclusions

A new MR image reconstruction method is presented. The proposed method exploits nonlocal similarity of image patches by establishing a patch-based nonlocal operator, PANO, which effectively produces sparse vectors by operating on grouped similar patches of the image. A reconstruction formulation is proposed to incorporate a sparsity constraint on PANO-produced coefficients, which can be considered as a generalization of previously proposed patch-based reconstruction methods. Simulation results based on fully sampled experimental data demonstrated consistent improvement in reconstruction accuracy of the proposed method over conventional CS-MRI reconstructions and several alternative CS-based reconstructions. We have also shown that the similarity information required by PANO can be iteratively learnt from a guide image reconstructed from undersampled k-space data and the proposed method is not sensitive to the initial guide image. In general, only learning the similarity twice is sufficiently enough to maximize the performance of the proposed method for the tested images. When the data are highly undesampled, learning the similarity from another contrast image with fully sampled data greatly improve the reconstruction.

Further improvement and verification on the methods may be made from the following aspects:

1) Designing a fomulation for joint similarity learning and image reconstruction. For example, one may consider to simultaneously learning of similarity for sparser representation and performing reconstruction with a surrogate function (Elad et al., 2007).

2) Speed up the imaging with non-Cartesian sampling. Radial (Block et al., 2007; Knoll et al., 2011) or spiral (Seeger et al., 2010) sampling may further accelerate the 2D imaging. But the availability of the guide image and how the gridding processes affect PANO should be carefully analyzed.

3) Coming PANO with partially parallel imaging (PPI). PPI has been widely adopted clinically and Poisson-disk acquisition can dramatically reduce the g-factor in 3D PPI (Lustig and Pauly, 2010; Vasanawala et al., 2010). One may combine PANO with PPI to

accelerate the imaging in practical applications. But how the sensitivity map affects the similarity matching should be carefully treated.

4) Test the method on more datasets acquired in real applications. All the comparisons in this paper are made on different slices of T2-weighted MR images acquired on the same volunteer. Given a specific MR clinical application, verification of the proposed method on more datasets acquired in real applications is worth of further investigation.

5) Joint reconstruction with undersampling of all multi-contrast images (Bilgic et al., 2011; Huang et al., 2012; Majumdar and Ward, 2011; Qu et al., 2011) and extend the PANO into multimodal imaging reconstruction, e.g. computer tomograph and MRI.

References

Adluru, G., DiBella, E.V.R., 2008. Reordering for improved constrained reconstruction from undersampled k-space data. Int. J. Biomed. Imaging. 2008. Article ID 341684.

Adluru, G., Tasdizen, T., Schabel, M.C., DiBella, E.V.R., 2010. Reconstruction of 3D dynamic contrast-enhanced magnetic resonance imaging using nonlocal means. J. Magn. Reson. Imaging 32, 1217-1227.

Akçakaya, M., Basha, T.A., Goddu, B., Goepfert, L.A., Kissinger, K.V., Tarokh, V., Manning, W.J., Nezafat, R., 2011. Low-dimensional-structure self-learning and thresholding: Regularization beyond compressed sensing for MRI Reconstruction. Magn. Reson. Med., 756-767.

Baker, C.A., King, K., Liang, D., Ying, L., 2011. Translational-invariant dictionaries for compressed sensing in magnetic resonance imaging, In: Proceedings of 8th IEEE International Symposium on Biomedical Imaging(ISBI'11), pp. 1602-1605.

Bao, L., Robini, M., Liu, W., Zhu, Y., 2013. Structure-adaptive sparse denoising for diffusion-tensor MRI.

Med. Image Anal. 17, 442–457.

Baraniuk, R., Choi, H., Neelamani, R., Ribeiro, V., Romberg, J., Guo, H., Fernandes, F., Hendricks, B., Gopinath, R., Lang, M., Odegard, J.E., Wei, D., 2009. Rice wavelet toolbox, http://dsp.rice.edu/software/rice-wavelet-toolbox.

Bilgic, B., Adalsteinsson, E., 2012. Joint Bayesian compressed sensing with prior estimate, In: Proceedings of 20th Scientific Meeting on International Society for Magnetic Resonance in Medicine (ISMRM'12), pp. 75.

Bilgic, B., Goyal, V.K., Adalsteinsson, E., 2011. Multi-contrast reconstruction with Bayesian compressed sensing. Magn. Reson. Med. 66, 1601-1615.

Block, K.T., Uecker, M., Frahm, J., 2007. Undersampled radial MRI with multiple coils. Iterative image reconstruction using a total variation constraint. Magn. Reson. Med. 57, 1086-1098.

Buades, A., Coll, B., Morel, J.M., 2005. A review of image denoising algorithms, with a new one. Multiscale Model Sim 4, 490-530.

Candes, E.J., Romberg, J., Tao, T., 2006. Robust uncertainty principles: Exact signal reconstruction from highly incomplete frequency information. IEEE Trans. Inform. Theory 52, 489-509.

Chen, C., Huang, J., 2012. Compressive sensing MRI with wavelet tree sparsity, Advances in Neural Information Processing Systems 25, pp. 1124-1132.

Chen, Y.M., Ye, X.J., Huang, F., 2010. A novel method and fast algorithm for MR image reconstruction with significantly under-sampled data. Inverse Probl Imag 4, 223-240.

Dabov, K., Foi, A., Katkovnik, V., Egiazarian, K., 2007. Image denoising by sparse 3-D transform-domain collaborative filtering. IEEE Trans. Image Process. 16, 2080-2095.

Dietrich, O., Raya, J.G., Reeder, S.B., Reiser, M.F., Schoenberg, S.O., 2007. Measurement of signal-to-noise ratios in MR images: Influence of multichannel coils, parallel imaging, and reconstruction filters. J. Magn. Reson. Imaging 26, 375-385.

Donoho, D.L., 2006. Compressed sensing. IEEE Trans. Inform. Theory 52, 1289-1306.

Egiazarian, K., Foi, A., Katkovnik, V., 2007. Compressed sensing image reconstruction via recursive spatially adaptive filtering, In: Proceedings of 14th IEEE International Conference on Image Processing (ICIP'07), pp. 549-552.

Elad, M., Matalon, B., Shtok, J., Zibulevsky, M., 2007. A wide-angle view at iterated shrinkage algorithms, In: Proceedings of Wavelets XII, August 26, 2007 - August 29, 2007. SPIE, San Diego, CA, USA.

Fang, S., Ying, K., Zhao, L., Cheng, J.P., 2010. Coherence regularization for SENSE reconstruction with a nonlocal operator (CORNOL). Magn. Reson. Med. 64, 1414-1426.

Gamper, U., Boesiger, P., Kozerke, S., 2008. Compressed sensing in dynamic MRI. Magn. Reson. Med. 59, 365-373.

Gho, S.M., Nam, Y., Zho, S.Y., Kim, E.Y., Kim, D.H., 2010. Three dimension double inversion recovery gray matter imaging using compressed sensing. Magn. Reson. Imaging 28, 1395-1402.

Haldar, J., Hernando, D., Liang, Z.P., 2011. Compressed-sensing MRI with random encoding. IEEE Trans. Med. Imaging 30, 893-903.

Henkelman, R.M., 1985. Measurement of signal intensities in the presence of noise in MR images. Med. Phys. 12, 232-233.

Hu, C.W., Qu, X.B., Guo, D., Bao, L.J., Chen, Z., 2011. Wavelet-based edge correlation incorporated iterative reconstruction for undersampled MRI. Magn. Reson. Imaging. 29, 907-915.

Huang, J. Z, Chen, C., Axel, L., 2012. Fast multi-contrast MRI reconstruction, In: Proceedings of 15th International Conference on Medical Image Computing and Computer Assisted Intervention (MICCAI'12), pp. 281-288.

Huang, J.Z., Yang, F., 2012. Compressed magnetic resonance imaging based on wavelet sparsity and nonlocal total variation, In: Proceedings of 9th IEEE International Symposium on Biomedical Imaging (ISBI'09), 968-971.

Huang, J.Z., Zhang, S.T., Metaxas, D., 2011. Efficient MR image reconstruction for compressed MR Imaging. Med Image Anal 15, 670-679.

Jung, H., Sung, K., Nayak, K.S., Kim, E.Y., Ye, J.C., 2009. k-t FOCUSS: A general compressed sensing framework for high resolution dynamic MRI. Magn. Reson. Med. 61, 103-116.

Knoll, F., Bredies, K., Pock, T., Stollberger, R., 2011. Second order total generalized variation (TGV) for MRI. Magn. Reson. Med. 65, 480-491.

Liang, D., Wang, H., Chang, Y., Ying, L., 2011. Sensitivity encoding reconstruction with nonlocal total variation regularization. Magn. Reson. Med. 65, 1384-1392.

Lingala, S.G., Hu, Y., DiBella, E., Jacob, M., 2011. Accelerated dynamic MRI exploiting sparsity and low-rank structure: k-t SLR. IEEE Trans. Med. Imaging 30, 1042-1054.

Lustig, M., Donoho, D., Pauly, J.M., 2007. Sparse MRI: The application of compressed sensing for rapid MR imaging. Magn. Reson. Med. 58, 1182-1195.

Lustig, M., Pauly, J.M., 2010. SPIRiT: Iterative self-consistent parallel imaging reconstruction from arbitrary k-space. Magn. Reson. Med. 64, 457-471.

Maggioni, M., Katkovnik, V., Egiazarian, K., Foi, A., 2013. Nonlocal transform-domain filter for volumetric data denoising and reconstruction. IEEE Trans. Image Process. 22, 119-133.

Majumdar, A., Ward, R.K., 2011. Joint reconstruction of multiecho MR images using correlated sparsity. Magn. Reson. Imaging 29, 899-906.

Manjón, J.V., Carbonell-Caballero, J., Lull, J.J., Garcia-Marti, G., Marti-Bonmati, L., Robles, M., 2008. MRI denoising using non-local means. Med. Image. Anal. 12, 514-523.

Manjón, J.V., Coupé, P., Buades, A., Louis Collins, D.L., Robles, M., 2012. New methods for MRI denoising based on sparseness and self-similarity. Med. Image Anal. 16, 18-27.

Manjón, J.V., Coupé, P., Buades, A., Collins, D.L., Robles, M., 2010. MRI superresolution using self-similarity and image priors. Int. J. Biomed. Imaging. 2010, Article ID 425891.

Ning, B.D., Qu, X.B., Guo, D., Hu, C.W., Chen, Z., 2013. Magnetic resonance image reconstruction using trained geometric directions in 2D redundant wavelets domain and non-convex optimization. Magn. Reson. Imaging 31, 1611–1622.

Otazo, R., Kim, D., Axel, L., Sodickson, D.K., 2010. Combination of compressed sensing and parallel imaging for highly accelerated first-pass cardiac perfusion MRI. Magn. Reson. Med. 64, 767-776.

Qu, X.B., Cao, X., Guo, D., Hu, C.W., Chen, Z., 2010a. Combined sparsifying transforms for compressed sensing MRI. Electron. Lett. 46, 121-122.

Qu, X.B., Guo, D., Ning, B.D., Hou, Y.K., Lin, Y.L., Cai, S.H., Chen, Z., 2012. Undersampled MRI reconstruction with patch-based directional wavelets. Magn. Reson. Imaging 30, 964-977.

Qu, X.B., Hu, C.W., Guo, D., Bao, L.J., Chen, Z., 2011. Gaussian scale mixture-based joint reconstruction of multicomponent MR images from undersampled k-space measurements, In: Proceedings of 19th Scientific Meeting on International Society for Magnetic Resonance in Medicine (ISMRM'11), pp. 2838.

Qu, X.B., Zhang, W.R., Guo, D., Cai, C.B., Cai, S.H., Chen, Z., 2010b. Iterative thresholding compressed sensing MRI based on contourlet transform. Inverse Probl. Sci. En. 18, 737-758.

Ravishankar, S., Bresler, Y., 2011. MR image reconstruction from highly undersampled k-space data by dictionary learning. IEEE Trans. Med. Imaging 30, 1028-1041.

Rousseau, F., 2010. A non-local approach for image super-resolution using intermodality priors. Med. Image Anal. 14, 594-605.

Seeger, M., Nickisch, H., Pohmann, R., Scholkopf, B., 2010. Optimization of k-space trajectories for compressed sensing by Bayesian experimental design. Magn. Reson. Med. 63, 116-126.

Shewchuk, J.R., 1994. An introduction to the conjugate gradient method without the agonizing pain. Carnegie Mellon University, Pittsburgh, PA, USA ,.

Trzasko, J., Manduca, A., 2009. Highly undersampled magnetic resonance image reconstruction via homotopic l_0-minimization. IEEE Trans. Med. Imaging 28, 106-121.

Trzasko, J.D., Haider, C.R., Borisch, E.A., Campeau, N.G., Glockner, J.F., Riederer, S.J., Manduca, A., 2011. Sparse-CAPR: Highly accelerated 4D CE-MRA with parallel imaging and nonconvex compressive sensing. Magn. Reson. Med. 66, 1019-1032.

Vasanawala, S.S., Alley, M.T., Hargreaves, B.A., Barth, R.A., Pauly, J.M., Lustig, M., 2010. Improved pediatric MR imaging with compressed sensing. Radiology 256, 607-616.

Wang, Y. L. , Yang, J. F., Yin, W. T. , Zhang, Y., 2008. A new alternating minimization algorithm for total variation image reconstruction. SIAM J. Imaging Sci. 1, 248-272.

Wong, A., Mishra, A., Fieguth, P., Clausi, D., 2013. Sparse reconstruction of breast MRI using Homotopic L_0 minimization in a regional sparsified domain. IEEE Trans. Biomed. Eng. 60, 743-752.

Wu, B., Millane, R.P., Watts, R., Bones, P.J., 2011. Prior estimate-based compressed sensing in parallel MRI. Magn. Reson. Med. 65, 83-95.

Yang, J.F., Zhang, Y., Yin, W. T., 2009. A fast TVL1-L2 minimization algorithm for signal reconstruction from partial Fourier data. Rice University, ftp://ftp.math.ucla.edu/pub/camreport/cam09-24.pdf.

Yang, J.F., Zhang, Y., Yin, W.T., 2010. A fast alternating direction method for TV l_1-l_2 signal reconstruction from partial Fourier data. IEEE J. Sel. Topics Signal Process. 4, 288-297.

Ying, D., Jim, J., 2011. Compressive sensing MRI with laplacian sparsifying transform, In: Proceedings of 8th IEEE International Symposium on Biomedical Imaging: From Nano to Macro (ISBI'11), pp. 81-84.

Zhao, B., Haldar, J.P., Christodoulou, A.G., Liang, Z.P., 2012. Image reconstruction from highly undersampled (k,t)-space data with joint partial separability and sparsity constraints. IEEE Trans. Med. Imaging 31, 1809-1820.

Zhuo, Y., Bradley, S., Wu, X.L., Haldar, J., Hwu, W.M., Liang, Z.P., 2010. Sparse regularization in MRI iterative reconstruction using GPUs, In: Proceedings of 3rd International Conference on Biomedical Engineering and Informatics (BMEI'10), pp. 578-582.